

Mesoporous Hydroxylated Carbon Nanofibers as an Effective Cathode Scaffold to Enhance the Lithiation-Delithiation Reversibility of Lithium-Sulfur Batteries

Faqi Yu, He Zhou, Yilin Li, Qiang Shen*

Key Laboratory for Colloid and Interface Chemistry of Education Ministry, School of Chemistry and Chemical Engineering, Shandong University, Jinan 250100, China.

*E-mail: qshen@sdu.edu.cn.

Received: 2 January 2018 / Accepted: 28 February 2018 / Published: 10 April 2018

Taking a reversible electrochemical reaction of elemental sulfur towards metallic lithium into consideration, it seems to be inappropriate to calculate Li^+ -ion diffusion coefficient (D_{Li}) within a solid-state cathode of carbon-sulfur composites using the concentration of lithium ions in electrolyte solution. In this paper, cross-linked non-porous carbon nanofibers (CNF) and mesoporous hydroxylated carbon nanofibers (m-HCNF) are prepared and comparatively utilized as sulfur-loading matrices to improve the lithiation-delithiation reversibility between molecular S_8 and metallic lithium. When model cells are assembled at a constant dosage of electrolyte (30 mL) per gram of sulfur, at open-circuit voltage the D_{Li} value of a lithium-sulfur (Li-S) battery cathode can be estimated according to the S_8 concentration therein: $3.51 \times 10^{-15} \text{ cm}^2 \text{ s}^{-1}$ for the low sulfur-loading cathode S/CNF (47.0 wt%); $4.21 \times 10^{-15} \text{ cm}^2 \text{ s}^{-1}$ for the high sulfur-loading electrode S/m-HCNF (~ 62.0 wt%). At 0.5 C the initial Coulombic efficiency of S/m-HCNF (96.9%) is higher than that of S/CNF (88.8%), and thereafter the better cycling stability and rate performance of the former coincide well with the varying D_{Li} values. In a word, these indicate an enhanced lithiation-delithiation reversibility of composite S/m-HCNF for high-performance Li-S batteries.

Keywords: Lithium-ion diffusion coefficient; Lithiation-delithiation reversibility; Mesoporous carbon nanofiber; Lithium-sulfur batteries.

1. INTRODUCTION

As an alternative to the presently commercial rechargeable lithium-ion batteries (LIBs), the energy storage system of lithium-sulfur (Li-S) battery has received great attention owing to the high theoretical capacity (1675 mAh g^{-1}), low cost and natural abundance of cathode sulfur [1-3]. Differing from the lithium intercalation-deintercalation mechanism of LIBs, Li-S battery works on the principle

of the reversible redox reaction between sulfur and lithium and thus faces great challenges such as the low electronic conductivity of sulfur ($5 \times 10^{-30} \text{ S cm}^{-1}$) and the high solubility of intermediate polysulfides (Li_2S_n , $4 \leq n \leq 8$) [4-10]. It is well-known that one of the most promising approaches is to develop porous carbonaceous materials for the complexing of conductive carbon and active sulfur [6, 11-27]. Apart from a high sulfur-loading amount, this porous carbonaceous framework with surface-dependent functional groups can not only shorten the diffusion route of lithium ions but also retard the shuttling effect of intermediate polysulfides.

It has been reported that the cross-linked networks of nitrogen/oxygen dual-doping carbon nanofiber (abbreviated as CNF), replicated from the same self-assemblies of polymeric polypyrrole (PPy), can be endowed with an interconnected, porous and channel-like nanostructure for the intercalation of lithium or for the loading of elemental sulfur or selenium [28-32]. When applied as cathode scaffolds of Li-S battery, the adsorption or confinement abilities of CNF's outside surface or inner voids, a robust mechanical feature of the electrochemically cycled frameworks, and even high-capacity properties of the carbon-sulfur composites, have been clearly demonstrated. As an example, the S-loading composite of N-doped microporous CNF webs can deliver a specific discharge capacity as high as 749.8 mAh g^{-1} at 0.2 C after 180 cycles [30]. Another example is the great progress in the activation and hydroxylation of these CNFs [32-34], therein the resulting micropores could serve as electrochemical reaction chambers and the N-/O-containing functional groups could effectively bind with sulfur and polysulfide species. Anyway, it is still a far way to achieve the practical application of these microporous CNFs as conductive scaffolds for high-performance Li-S battery cathodes.

In Li-S batteries, the reversible electrochemical reaction between elemental sulfur and metallic lithium should also deal with Li^+ -ion diffusions in electrolyte solution, across the interface between solution-state electrolyte and solid-state electrode and within the non-lithium intercalated cathode. Even if the electrochemical reaction in Li-S battery is an ion-diffusion controlling process, it seems to be inappropriate to calculate Li^+ -ion diffusion coefficient (D_{Li}) within a working electrode using the concentration of lithium ions in the electrolyte solution. Actually, according to the concentration of Li^+ ions in electrolyte, the obtained D_{Li} values in literature reports [7, 22, 35, 36] are at the 10^{-8} - 10^{-10} order of magnitude, which are much bigger than that of carbon-coated LiFePO_4 cathode at the 10^{-12} order of magnitude [37]. Therefore, how to precisely evaluate and to improve the Li^+ -ion diffusion in porous CNF-sulfur composite should be of crucial importance presently.

In this paper, the cross-linked networks of polypyrrole nanofiber (PPy-NF) were prepared and then used as precursors to derive cross-linked non-porous CNF and mesoporous hydroxylated carbon nanofiber (m-HCNF) by the simple carbonization and combined carbonization/activation routes, respectively. After the sulfur-loading at the carbon/sulfur mass ratio of 1:2, the resulting S/m-HCNF composite possesses a sulfur weight percentage of 62.0 wt%, higher than that (47 wt%) of composite S/CNF. When applied as Li-S battery cathodes at a dosage of 30 mL per gram of sulfur, composite S/m-HCNF delivers a reversible capacity of 884.1 mAh g^{-1} at 0.5 C in the 150th cycle, higher than that (599.3 mAh g^{-1}) of S/CNF composite electrode operated at the same conditions. Comparing to the obtained electrochemical parameters (e.g., the internal resistances and the D_{Li} value) of S/CNF, the enhanced reaction reversibility of molecular S_8 in composite S/m-HCNF with metallic lithium could be reasonably highlighted. Aside from the structural properties of the two modified CNFs and their

composites with sulfur, the lithiation-delithiation reversibility of elemental sulfur was focused and discussed in detail in context.

2. EXPERIMENTAL

2.1. Materials and precursor preparation

All the chemicals, such as sodium persulfate ($\text{Na}_2\text{S}_2\text{O}_8$), concentrated aqueous solution of hydrochloric acid (HCl, 36-38%), hexadecyl trimethyl ammonium bromide (CTAB), pyrrole (Py) monomer and sublimed sulfur, are of analytical grade and were used without further purification. Ultrapure water (18.25 M Ω cm) was used throughout solution preparation and sample rinse.

Cross-linked polypyrrole nanofibers (PPy-NF) were synthesized via a modified oxidative template assembly route [38]. In a typical procedure, CTAB (1.092 g) and $\text{Na}_2\text{S}_2\text{O}_8$ (2.142 g) were sequentially added into a dilute HCl aqueous solution (60 mL, 1.0 M) under ice bath (0 - 3 °C), forming the white reactive templates via a magnetic stirring. Then, Py monomer (0.83 mL) was added into the ice-bath reactor, and its template polymerization was performed for 24 h. And then, the black precipitate of PPy-NF was thoroughly washed with water and then absolute alcohol, dried at 80 °C in an oven for 24 h, and treated as a precursor for the next carbonization processing.

2.2. Modification and sulfur-loading of PPy-NF

Under nitrogen atmosphere the precursor sample of PPy-NF was heated at a rate of 5 °C min⁻¹ and then kept at 700 °C for 2 h. The only carbonization of PPy-NF induces the formation of cross-linked non-porous carbon nanofibers, defined as the comparative sample of CNF.

At first, solid-state PPy-NF (500 mg) was dispersed into KOH aqueous solution (1 M, 9 mL), soaked for 1 h, and dried at 80 °C for 12 h. And then, the solid-state admixture of KOH and PPy-NF was heat-treated at 700 °C for 2 h under nitrogen atmosphere. Finally, the activated PPy-NF was thoroughly washed using aqueous HCl (60 mL, 1 M) and then water until pH~7.0. After drying at 80 °C for 24 h, the target sample of mesoporous hydroxylated carbon nanofibers was obtained, referred to as m-HCNF.

As-obtained CNF (or m-HCNF) and sublimed sulfur were mixed at a mass ratio of 1 : 2, ground in an agate mortar for 10 min, transferred into a porcelain crucible and heat-treated using N₂ flow (~50 mL min⁻¹) at 155 °C for 10 h [39]. Correspondingly, the sulfur-loading sample was defined as the comparative S/CNF (or the target S/m-HCNF) composite.

2.3. Structural characterization

Scanning electron microscopy (SEM) and Transmission electron microscopy (TEM) were carried out on a JEOL JSM-6700F (10 kV) and JEOL JEM 2100 (200 kV) microscopes, respectively. Elemental analysis on the surface of sample was identified by X-ray energy dispersive spectroscopy

(EDS). Nitrogen adsorption isotherms were measured on a micromeritics ASAP 2020 porosimeter at 77 K using a 10-second equilibrium interval. Thermogravimetric analysis (TGA) measurements were conducted on a Mettler Toledo TGA/SDTA851 machine with a heating rate of 10 °C min⁻¹ under N₂ atmosphere. X-ray diffraction (XRD) patterns were recorded on a Rigaku D/max 2400 kV powder X-ray diffractometer with Cu K α radiation ($\lambda = 1.5406 \text{ \AA}$) in the 2 θ range of 10 and 70°. Raman spectra were measured using a LABRAM-HR confocal laser micro-Raman spectrometer (632.8 nm). X-ray photoelectron spectroscopy (XPS) analysis was performed on a VG Scientific ESCALAB 220i-XL electron spectrometer using Al K α radiation.

2.4. Electrochemical characterization

After the thoroughly mixing of S/CNF (or S/m-HCNF) composite (70 wt%), acetylene black (20 wt%) and sodium alginate (10 wt%), the homogeneous slurry was pasted onto an aluminum foil and dried at 60 °C for 12 h. And then, the foil was cut into discs with a diameter of 12 mm, and used as working electrodes with a sulfur loading of $1.0 \pm 0.2 \text{ mg cm}^{-2}$. Lithium metal, nickel foam and Celgard 2300 were used as counter electrode, current collector and separator, respectively. 1.0 M Lithium bis-(trifluoromethanesulfonyl) imide (LiTFSI) in a mixed solvent of 1, 3-dioxanes and 1, 2-dimethoxyethane (1 : 1, vol : vol) with 2 wt% LiNO₃ was used as electrolyte at a dosage of 30 mL per gram of sulfur. CR2032-type coin cells were assembled in an argon-filled glove box prior to electrochemical measurements.

Galvanostatic charge-discharge tests were conducted on a Land CT2001A battery system within a narrow potential range of 1.8 and 2.7 V vs. Li⁺/Li and *ibid.* Cyclic voltammetry (CV) performances were carried out on an LK 2005A Electrochemical Workstation at 0.1 mV s⁻¹ in the voltage range of 1.5-3.0 V. Electrochemical impedance spectroscopy (EIS) measurements were conducted in the frequency range from 100 kHz to 100 mHz with the AC voltage amplitude of 5 mV. It should be mentioned that galvanostatic cycling tests were performed at 30 °C and the others were operated at room temperature.

3. RESULTS AND DISCUSSION

3.1. Modified structural characteristics of S/m-HCNF composite

As schematically shown in Figure 1, at first as-obtained PPy-NF was subjected to a carbonization, or a KOH-assisted carbonization/activation, at 700°C for 2 h under N₂ flow (~100 mL min⁻¹) atmosphere. Then, the cross-linked PPy-NF derived carbon nanofibers (CNF), or the porous hydroxylated carbon nanofibers (m-HCNF), was treated as conductive matrix to load elemental sulfur (*i.e.*, molecular S₈) via melt-diffusion route at 155°C. And then, the frameworks CNF and m-HCNF, as well as their sulfur-loading counterparts of S/CNF and S/m-HCNF composites, were comparatively assayed to clarify advantages of the experimental design of m-HCNF as effective cathode scaffolds to improve the electrochemical reaction reversibility of molecular S₈ towards metallic lithium.

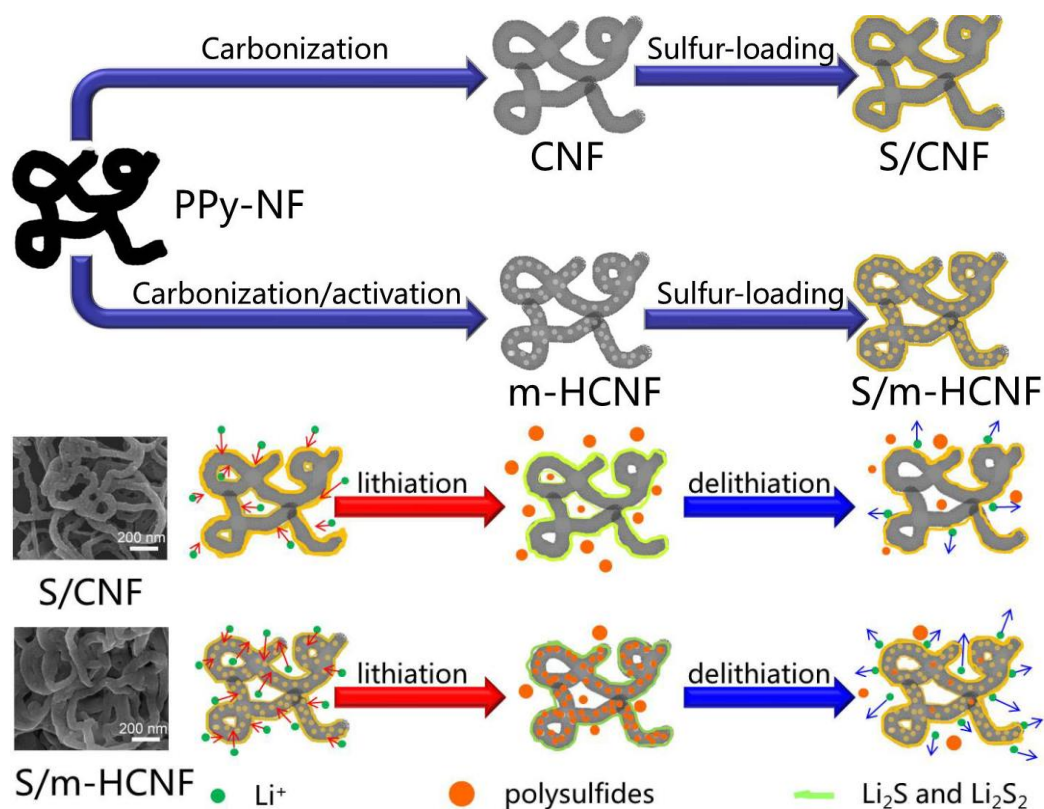


Figure 1. Schematic illustration of the experimental procedure adopted (a) for the preparation of S/CNF and S/m-HCNF composites and (b) for their comparative lithiation-delithiation reversibility of elemental sulfur towards metallic lithium.

Herein, only the high-temperature carbonization at 700°C could simply replicate the cross-linked nanofiber webs of precursor PPy-NF in morphology [28, 30, 38], resulting in CNF with an average size of ~75 nm in diameter (Figure 2a and 2b). By comparison, the simultaneous carbonization and activation of PPy-NF nanofibers could irregularly “destroy” the cross-linked network structure (i.e., the circular meshes) and shorten/roughen these nanofibers to produce the porous scaffolds of m-HCNF (Figure 2c and 2d). Considering the pore-punching effectiveness of additive KOH, the subsequent sulfur-loading exerts almost no influence on the morphology of the porous carbon-based nanofibers m-HCNF (Figure 2c-f). SEM and the corresponding elemental mapping images of composite S/m-HCNF clearly demonstrate the coexistence and homogeneous distribution of C, N, O and S elements (Figure 2g and 2h), indicating that most of the elemental sulfur localizes within the porous structure of N-/O-containing carbonaceous framework m-HCNF. As for S/CNF composite, the subsequent sulfur-loading clearly made the nanofiber surface of CNF becoming rough, indicating the random deposition of molecular S₈ on the surface (Figure 3).

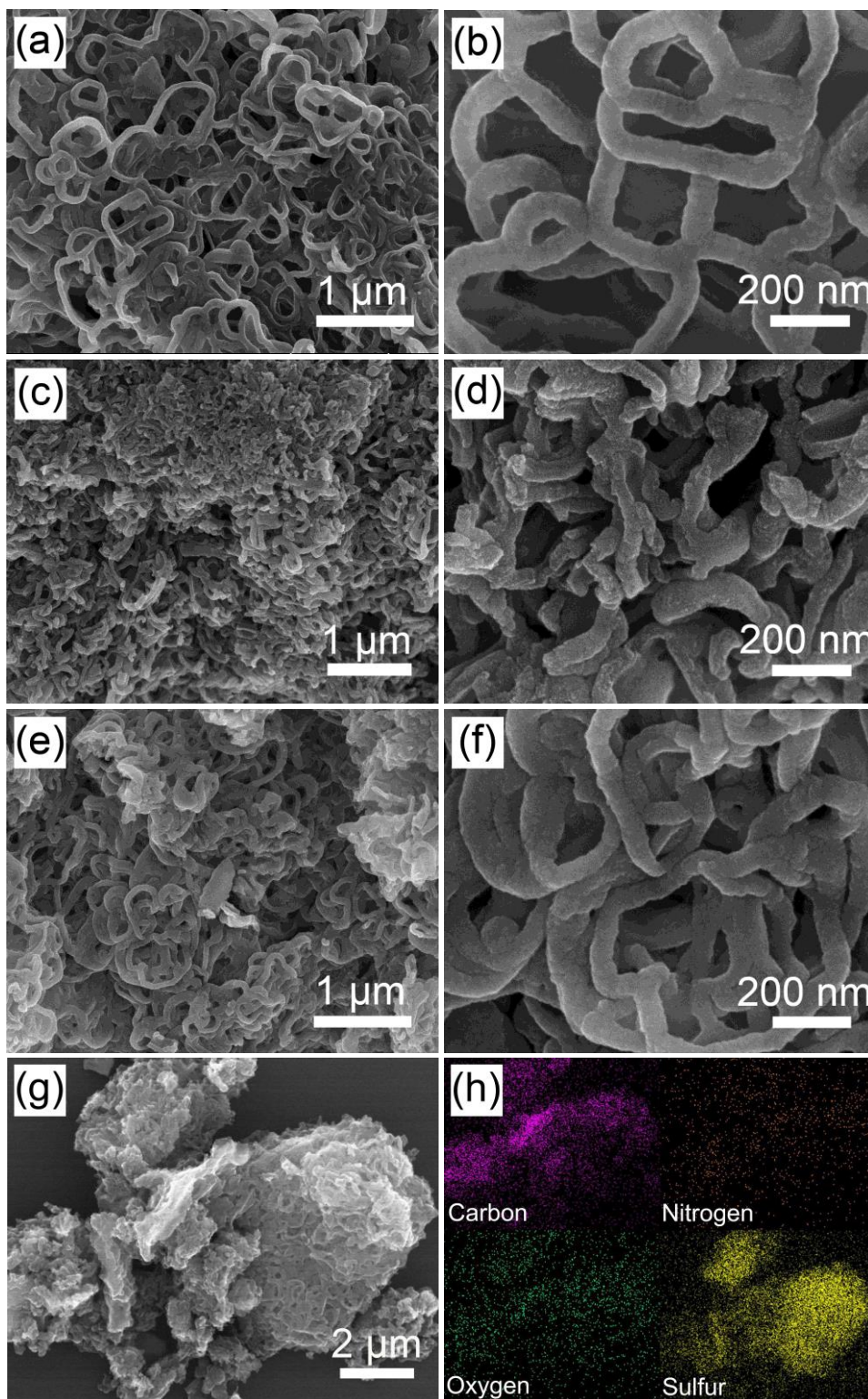


Figure 2. SEM images of (a, b) CNF and (c, d) m-HCNF scaffolds and (e-g) S/m-HCNF composite. (h) Elemental mapping images of composite S/m-HCNF shown in panel (g).

It is similar to Figure 2a and 2b that TEM image of CNF cross-linked nanofibers clearly exhibits the circular meshes (Figure 4a), and each fiber acquires the hollow-like and non-porous structure by the merely high-temperature carbonization (Figure 4b).

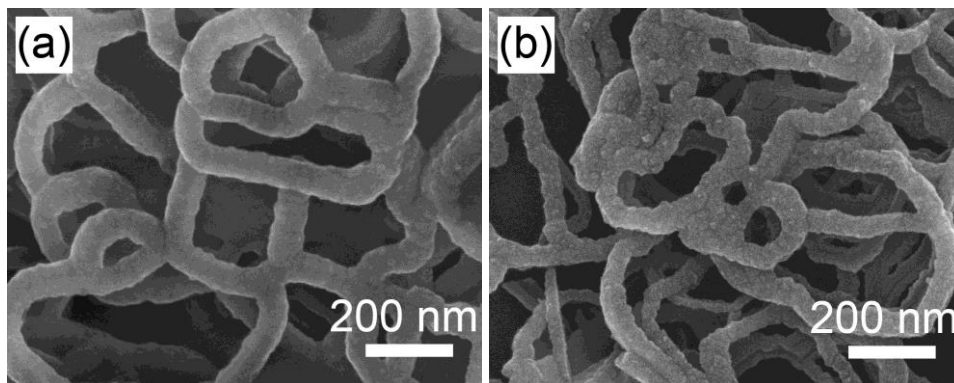
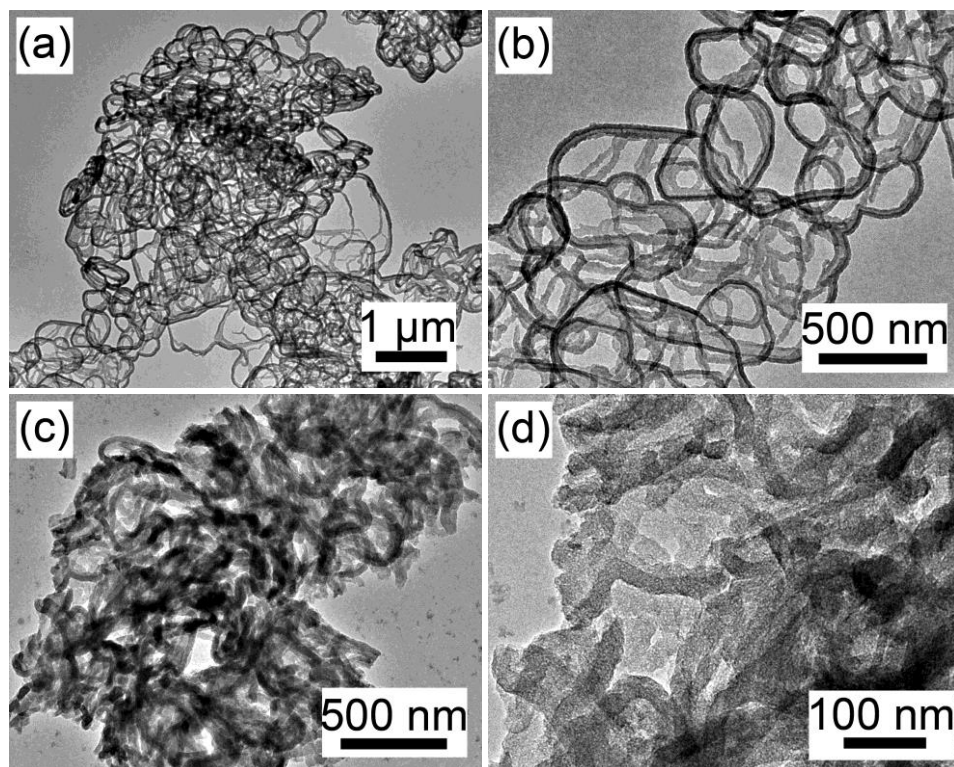


Figure 3. SEM images of (a) CNF and (b) S/CNF composite.

Owing to the simultaneous activation of chemical KOH, the network nodes of precursor PPy-NF were “opened” for the resulting porous material m-HCNF (Figure 4c). By high-resolution TEM, the white spots for the visually determined mesoporous structure of m-HCNF could be detected (Figure 4d). Probably, thanks to both the surface adsorption of elemental sulfur and its sufficient infiltration into the inner voids of the carbon-based matrices, the porous and nanofiber-shaped structure of scaffold m-HCNF could hardly be recognized for S/m-HCNF composite (Figure 4e). By focusing electron beam on a selected area of the composite, the obtained electron diffraction pattern reveals the amorphous nature of composite S/m-HCNF or its component sulfur (Figure 4f).



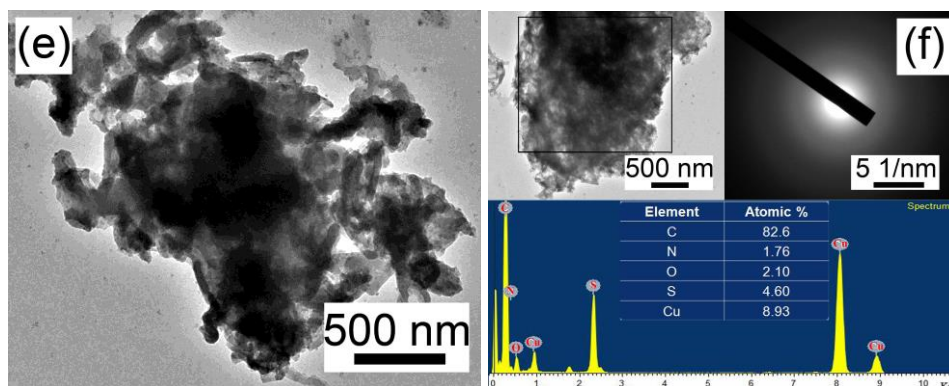
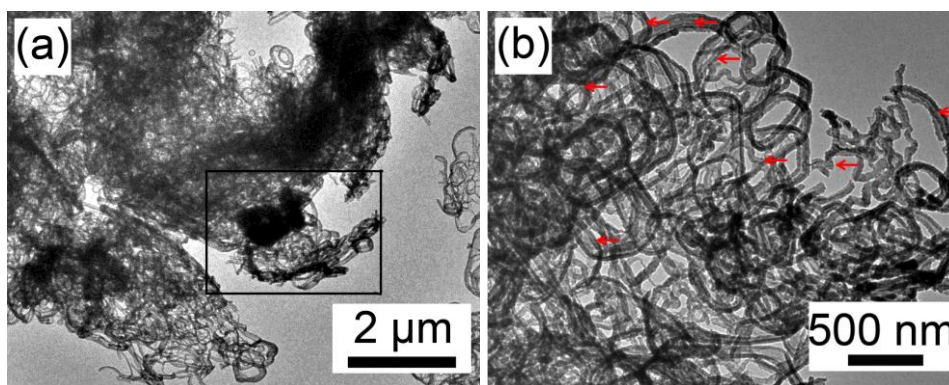


Figure 4. TEM images of (a, b) CNF and (c, d) m-HCNF scaffolds and (e) S/m-HCNF composite. (f) TEM image and the corresponding electron diffraction pattern and EDS analyses of composite S/m-HCNF.

Two situations should be mentioned to demonstrate that only the surface adsorption dominates the sulfur-loading of non-porous CNF cross-linked nanofibers for the formation of composite S/CNF. The one is that, as reported by Manthiram et al [30, 32, 38], there exist N-/O-containing functional groups for these PPy-NF-derived multichannel carbon nanofibers even without the assistance of activating agents and these surface-pendent functional groups can strongly interact with elemental sulfur. Another one is that, at least, the hollow-like structure of pristine CNF (Figure 4b) could be partly preserved in composite S/CNF (Figure 5a, 5b). As marked by the red arrows in Figure 5b, there still exist hollow channels in S/CNF composite after sulfur-loading. This indicates that parts of the channels are closed at least, or, the infiltration of molecular S_8 into these channels could be omitted.

Along with TEM observation, the corresponding electron diffraction pattern and EDS analyses further prove the successfully complexing of framework CNF with crystalline S_8 nanoparticles for the formation of composite S/CNF (Figure 5c, 5d). According to the comparative EDS analyses, the sulfur-to-carbon atomic ratios (i.e., S/C, atom%/atom%) of composites S/CNF ($\sim 0.6/87.1$) and S/m-HCNF ($\sim 4.6/82.6$) further indicate the much more amount of elemental sulfur was encapsulated by the m-HCNF (Figure 4f, 5d).



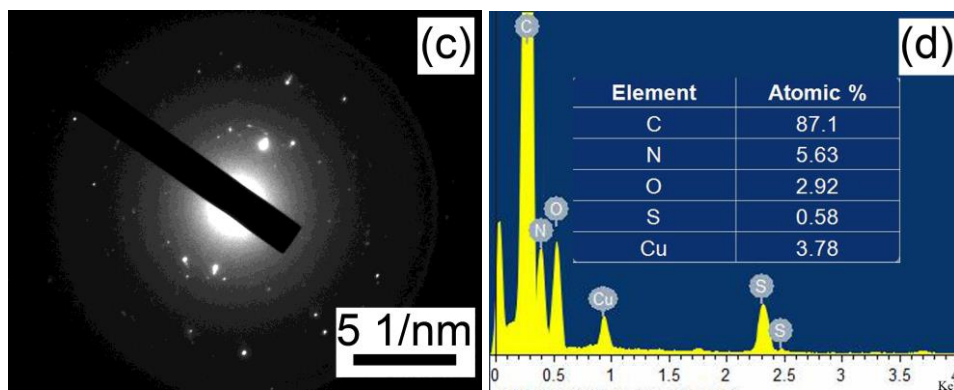


Figure 5. (a, b) TEM images of S/CNF composite. (c) Electron diffraction pattern and (d) corresponding EDS results of the selected area marked in panel (a).

Nitrogen adsorption-desorption measurement of m-HCNF nanofibers gives a high specific surface area of $1808.9 \text{ m}^2 \text{ g}^{-1}$ and a high pore volume of $1.77 \text{ cm}^3 \text{ g}^{-1}$, and the isotherms are close to a combination form of type I and type IV (Figure 6a). In the N_2 adsorption-desorption isotherms of m-HCNF, although the N_2 sharp uptake at a low pressure ($P/P_0 \sim 0$) or the N_2 uptake tail at a high pressure ($P/P_0 > 0.97$) indicates the existence of micropores or macropores, the relatively big type H4 hysteresis loop appearing within the medium pressure region illustrates the main presence of mesopores for these porous nanofibers. Furthermore, the major mesoporous feature of m-HCNF nanofibers with an average pore diameter of 3.3 nm could be demonstrated (Figure 6b), which is consistent with the visually determined results of Figure 4d. By comparison, the acquired specific surface area (i.e., $192.5 \text{ m}^2 \text{ g}^{-1}$) and pore volume (i.e., $0.42 \text{ cm}^3 \text{ g}^{-1}$) are relatively small for the non-porous structure of CNF cross-linked nanofiber webs.

TGA analyses of composites S/CNF and S/m-HCNF could comparatively announce the S-loading capabilities of scaffolds CNF and m-HCNF (Figure 6c and 6d). TG behavior of either CNF or m-HCNF displays an initial weight loss below $100 \text{ }^\circ\text{C}$ and a subsequent weight loss between 100 and $450 \text{ }^\circ\text{C}$ (Figure 6c or 6d), assigned to the evaporation of absorbed water and the partial thermal decomposition of the carbonaceous matrix, respectively. In Figure 6c or 6d, the total weight loss of 48.9 (S/CNF) or 64.3 wt% (S/m-HCNF) was determined, and then by eliminating the effect of the corresponding scaffold, sulfur contents in composites S/CNF (47.0 wt%) and S/m-HCNF (62.0 wt%) could be calculated. Therefore, these further assure the advantage of KOH-assisted carbonization/activation to generate m-HCNF with a high surface-area-to-volume ratio for the closer contact with electrolyte.

Each XRD pattern of scaffolds CNF, m-HCNF and composites S/CNF, S/m-HCNF predominantly presents a reflection band around 23° , attributed to the mainly amorphous nature of them. In Figure 6e, one exception is the two diffraction bands, around 23° and 43° , of scaffold m-HCNF that coincide well with the (002) and (100) planes of graphitic carbon in sequence, which indicates the layered arrangement of the partial graphitized m-HCNF with an interlayer spacing of 3.85 \AA larger than that of graphite (i.e., 3.35 \AA). Especially, this is favorable for the electrochemical diffusion of lithium ions when applied as a cathode scaffold of Li-S batteries [40]. When sublimed

sulfur was heat-treated at 155 °C for 10 h, the resulting S-treated sample possesses the exactly same XRD pattern as that of elemental sulfur (orthorhombic crystals, JCPDS No. 08-0247). This indicates a high thermal stability of molecular S₈ (Figure 6e). Another exception is the diffraction peaks of orthorhombic sulfur crystals appearing in the XRD pattern of S/CNF composite, which prove that S₈ crystallites localize at the surface of non-porous CNF.

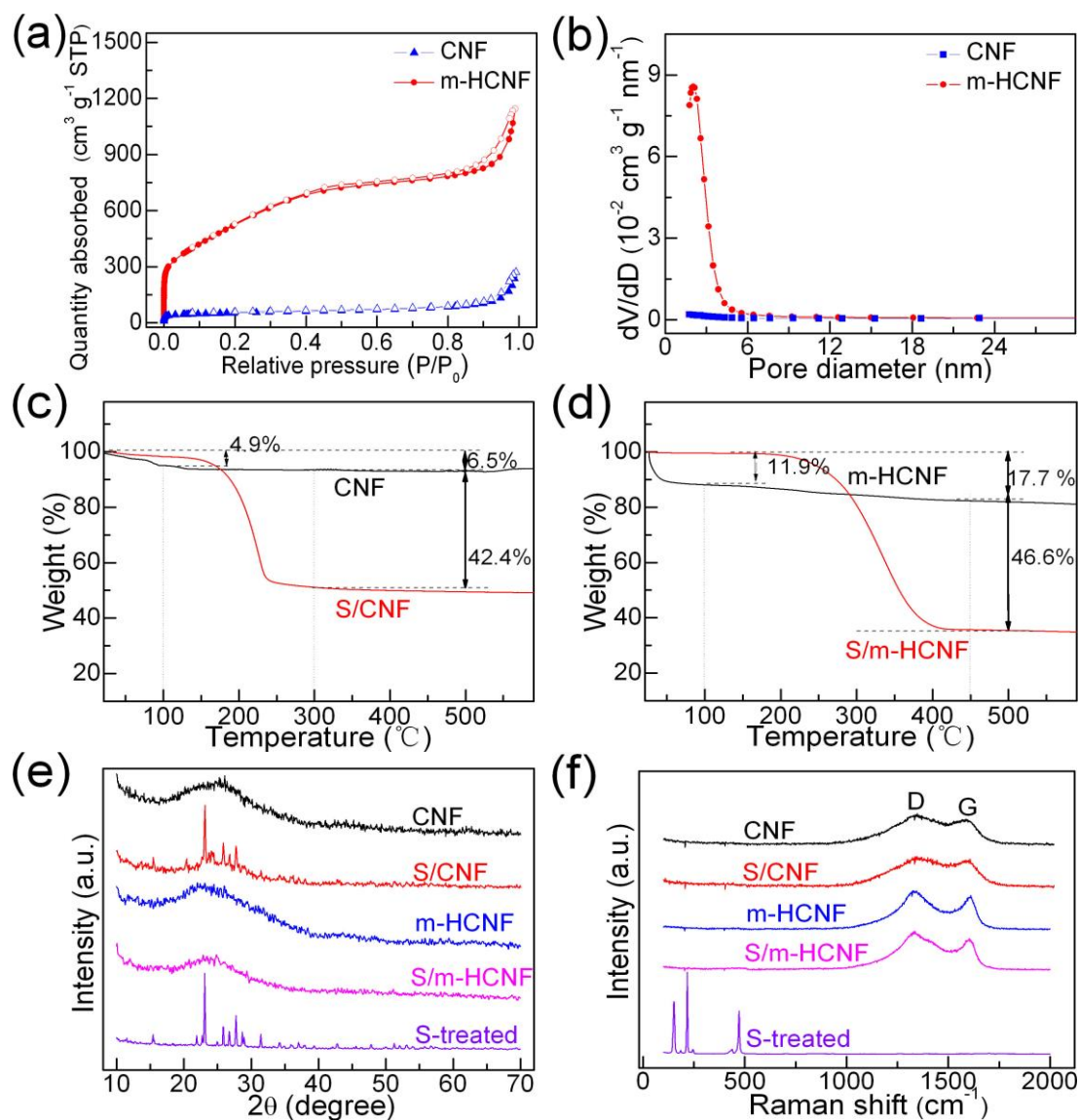


Figure 6. (a) N₂ adsorption-desorption isotherms and (b) pore size distributions of scaffolds CNF and m-HCNF. (c, d) TGA curves, (e) XRD patterns and (f) Raman spectra of scaffolds CNF and m-HCNF and their S-loading composites S/CNF and S/m-HCNF, and in panel (e) or (f) the characteristics of S-treated sample is also enclosed.

Raman spectra of S-treated, CNF, m-HCNF, S/CNF and S/m-HCNF samples were comparatively shown in Figure 6f, revealing the typical characteristics of a partially graphitized carbon: a disordered D band at 1325 cm⁻¹ and an in-plane vibrational G band at 1610 cm⁻¹. Moreover, the Raman peak intensity ratio of D to G band (i.e., I_D/I_G) is 1.13 for scaffold m-HCNF, while that is

1.25 for composite S/m-HCNF. This indicates that the structure of S/m-HCNF composite is highly defective by comparison with that of the m-HCNF [41]. Differing from the XRD results shown in Figure 6e, Raman peaks of elemental sulfur could not be detected for composite S/CNF (Figure 6f). Probably, the strong interactions between S_8 molecules and the surface-pendent functional groups of scaffold CNF could substantially weaken the Raman signals of crystalline sulfur therein.

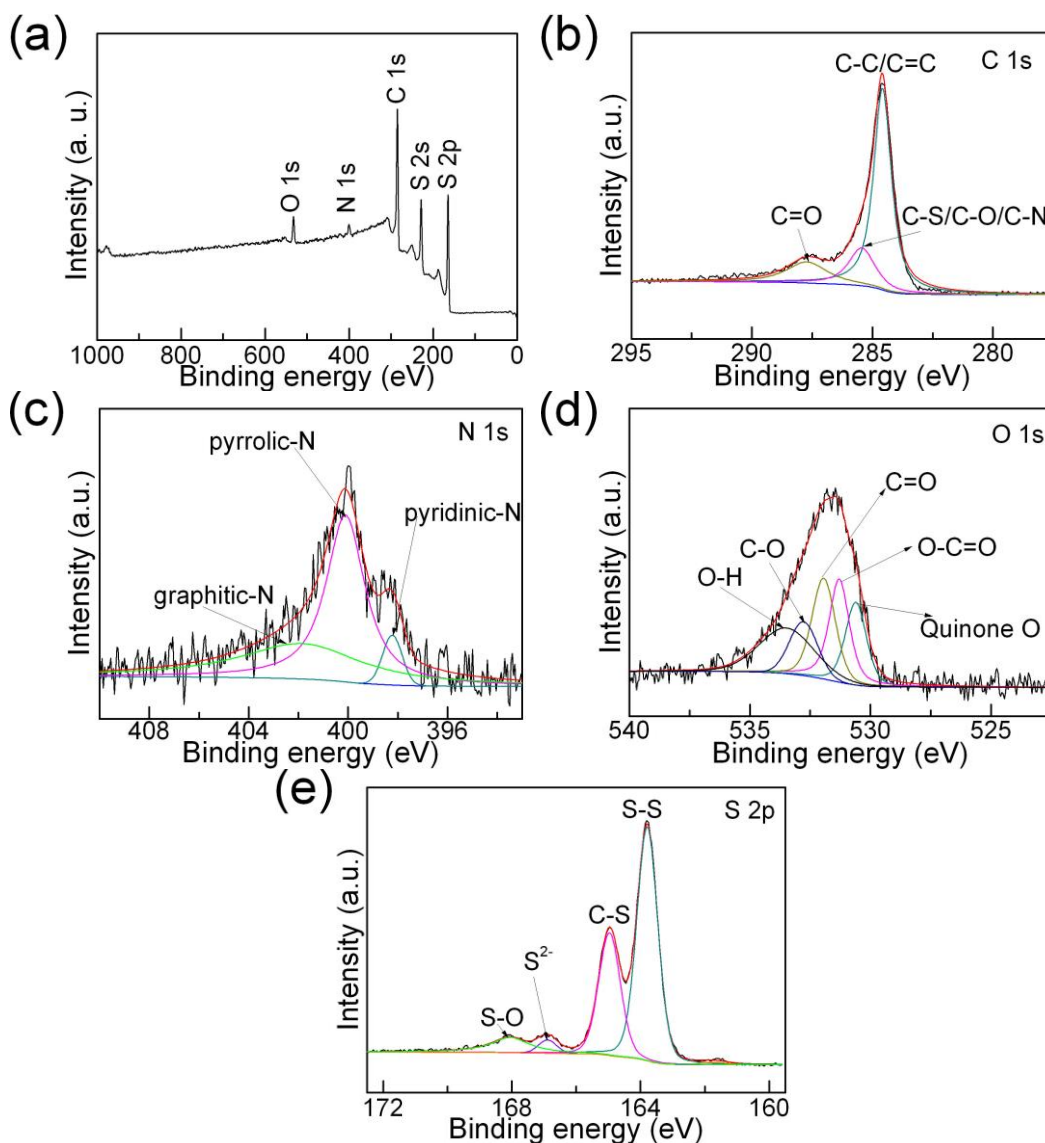


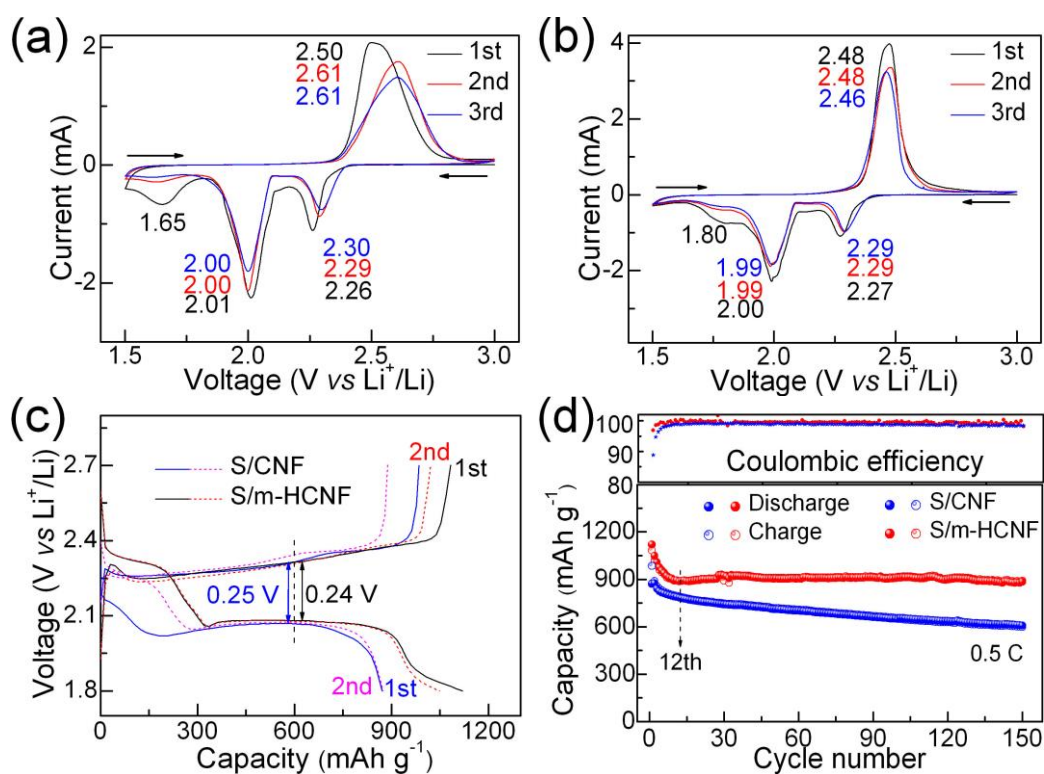
Figure 7. (a) Overall, (b) C 1s, (c) N 1s, (d) O 1s and (e) S 2p XPS spectra of S/m-HCNF composite, respectively.

Overall XPS spectrum of composite S/m-HCNF proves the coexistence of C, N, O, and S elements, and the corresponding N 1s and O 1s refinements further indicate the possible species of N/O-containing functional groups (Figure 7). In the C 1s XPS spectrum of Figure 7b, the highest three signals at 284.7, 286.0 and 287.4 eV may originate from the chemical bonds of C-C/C=C, C-S/C-O/C-N and C=O [22, 42]. As shown in Figure 7c, N 1s spectrum and the fitting results reveal three nitrogen

species: pyridinic-N (398.2 eV), pyrrolic-N (400.1 eV) and graphitic-N (401.9 eV). As marked in the O 1s XPS spectrum of Figure 7d, five peaks at 530.6, 531.3, 531.9, 532.8 and 533.5 eV can be assigned to quinone O, O-C=O, C=O, C-O and O-H species in sequence. While in the S 2p spectrum of Figure 7e, the four peaks at 163.8, 165.0, 166.9 and 168.1 eV can be ascribed to S-S, C-S, S²⁻ and S-O species in sequence [32, 43, 44]. It is expected that, aside from the substantial ability to adsorb/confine elemental sulfur and intermediate polysulfides, these functional groups could improve electrical conductivity of the composite [45].

3.2 Enhanced Li⁺-ion transfer in S/m-HCNF composite electrode

Within the potential range of 1.5 and 3.0 V at 0.1 mV s⁻¹, initial three CV curves of S/CNF and S/m-HCNF composite electrodes are shown in Figure 8a and 8b, respectively. As for the composite S/CNF in the 1st cycle, its gradual lithiation reactions show two distinctive reduction peaks at 2.26 and 2.01 V, being attributed to the reductions of molecular S₈ to electrolyte-soluble intermediate polysulfides (Li₂S_n, 4 ≤ n ≤ 8) and then to the insoluble Li₂S/Li₂S₂ in sequence (Figure 8a). Subsequently, the 1st reverse delithiation of elemental sulfur exhibits a relatively broad oxidation peak around 2.50 V for the gradual transformation of Li₂S/Li₂S₂ to molecular S₈. If the potential gap (ΔE_{a/c}) between this anodic peak and the low-potential cathodic peak (i.e., 2.50 - 2.01 = 0.49 V) could be treated as a parameter to denote the electrochemical reversibility of the full lithiation-delithiation process, the bigger of the ΔE_{a/c} value in each cycle and the higher of electrode polarization wherein. As marked in Figure 8a, in the 2nd CV cycle and thereafter, the bigger potential difference of redox peaks (i.e., ΔE_{a/c} value ~ 0.61 V) could be assigned to the already irreversible formation of interphase between solid-state electrode and solution-state electrolyte (i.e., SEI layer) in the 1st cycle [46].



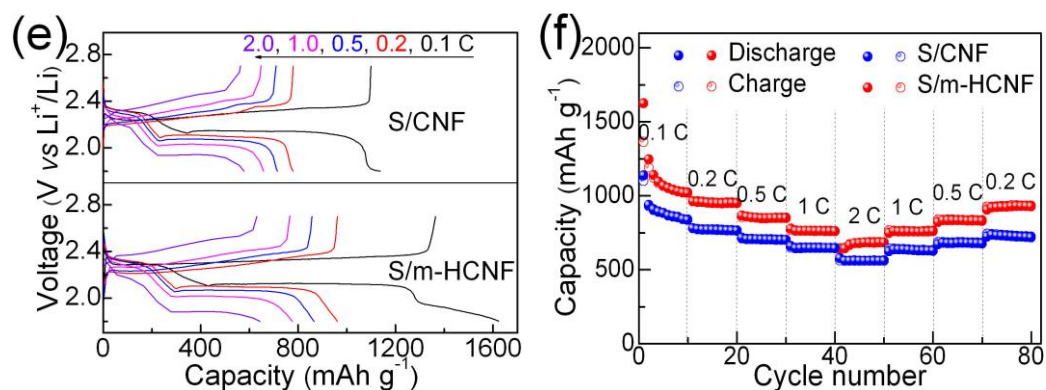


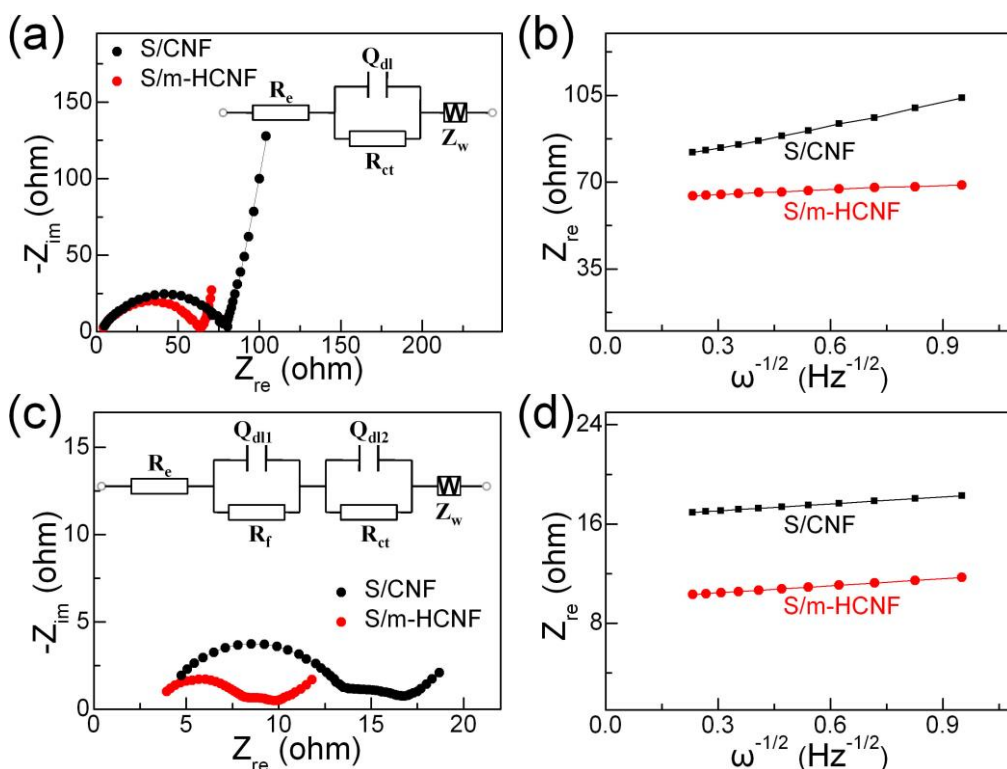
Figure 8. Electrochemical behaviors of S/CNF and S/m-HCNF electrodes: (a, b), CV curves at a scanning rate of 0.1 mV s^{-1} ; (c, d) voltage profiles and cycling stabilities at 0.5 C ; (e, f) voltage profiles and rate capabilities of S/CNF and S/m-HCNF at various current rates.

As for the CV behaviors of a S/m-HCNF composite electrode (Figure 8b), the initial cathodic/anodic scanning gives almost the same $\Delta E_{a/c}$ value (0.48 V) as that of S/CNF electrode, implying a similar lithiation-delithiation mechanism of molecular S_8 occurring in the 1st cycle. However, the $\Delta E_{a/c}$ value of composite S/m-HCNF slightly increases to 0.49 V in the 2nd cycle and then slightly decreases to a constant of 0.47 V in the 3rd cycle and thereafter. By comparison, in the 2nd cycle and thereafter the higher electrode polarization ($\Delta E_{a/c} \sim 0.61 \text{ V}$) of composite S/CNF (S-loading $\sim 47.0 \text{ wt}\%$) could be assigned to the limited ability of non-porous scaffold CNF for the surface adsorption of intermediate polysulfides Li_2S_n (Figure 8a), whereas the lower electrode polarization ($\Delta E_{a/c} \sim 0.47 \text{ V}$) of composite S/m-HCNF (S-loading $\sim 62.0 \text{ wt}\%$), in the 3rd cycle and thereafter, is associated with the high specific surface area of mesoporous scaffold m-HCNF to adsorb/confine sulfur-containing species immensely.

In each voltage profile of S/CNF and S/m-HCNF composite electrodes recorded at a current rate of 0.5 C ($1 \text{ C} = 1675 \text{ mA g}^{-1}$), two discharge voltage plateaus are obviously distinguishable (Figure 8c), which coincides well with the two cathodic peaks in the corresponding CV behaviors. Composite S/CNF exhibits a discharge/charge capacity of $985.0/871.8 \text{ mAh g}^{-1}$ in the 1st cycle, while cathode S/m-HCNF delivers a discharge/charge capacity of $1120.0/1082.6 \text{ mAh g}^{-1}$ therein. Also in Figure 8c, the reversible capacity in the 2nd cycle and the initial Coulombic efficiency of composite S/m-HCNF are as high as $1049.3 \text{ mAh g}^{-1}$ and 96.9% , much higher than those of cathode S/CNF (i.e., 874.6 mAh g^{-1} , 88.8%). In the 2nd cycle and even in each cycle thereafter, an irreversible capacity fade has been generally assigned to the presence of electrolyte-soluble Li_2S_n ($4 \leq n \leq 8$) and its subsequently back and forward shuttling [47]. And, this seems to conflict with the same electrochemical reaction mechanism between molecular S_8 and metallic lithium at a constant dosage of electrolyte (30 mL) per gram of sulfur (i.e., the possibly constant concentration of Li_2S_n in electrolyte solution). As marked in Figure 8c, the voltage difference between the discharge and charge plateaus of S/CNF (0.25 V) is slightly bigger than that of composite S/m-HCNF (0.24 V), and probably, the bigger is the voltage difference and the higher concentration is the intermediate Li_2S_n ($4 \leq n \leq 8$) in electrolyte solution.

As for the comparative S/CNF cathode operated at 0.5 C, the galvanostatic cycling may cause the formation of the intermediate Li_2S_n ($4 \leq n \leq 8$) in each cycle and thus the corresponding irreversible capacity decay could gradually increase along with the increasing cycle number (Figure 8d). Within the initial 12 charge-discharge cycles at 0.5 C, the continuously penetrating of electrolyte into the mesoporous electrode may gradually activate composite S/m-HCNF and thus its reversible capacity decreases with the increasing cycle number (Figure 8d). Thereafter, even if the high specific surface area of porous scaffold m-HCNF does hardly functionalize for the surface adsorption of the intermediate Li_2S_n ($4 \leq n \leq 8$), the positive volume-buffering effect of the inner mesopores, as well as their confinement of the gradually formed intermediate Li_2S_n ($4 \leq n \leq 8$), may functionalize predominantly. Therefore, at 0.5 C the reversible capacity of S/m-HCNF electrode gradually decreases from the 2nd (1049.3 mAh g^{-1}) to the 12th cycle (887.2 mAh g^{-1}) and keeps almost unchanged thereafter, reaching a high residual value of 884.1 mAh g^{-1} in the 150th cycle (Figure 8d).

Compared to the S/CNF cathode, the mesoporous structure of scaffold m-HCNF can shorten the pathway of Li^+ -ion diffusion, comparatively corresponding to a superior rate capability of composite S/m-HCNF. When operating current rate was gradually changed from 0.1 C to 0.5 C and then to 2.0 C, the discharge capacities of the S/m-HCNF electrode are 1017.6, 848.6 and 682.3 mAh g^{-1} in sequence, higher than those of composite S/CNF correspondingly (Figure 8e, 8f). And then, when the current rate gradually goes back to 0.2 C, the specific capacity of cathode S/m-HCNF recovers to a high value of 905.0 mAh g^{-1} (Figure 8f). In some senses, both the relatively good cycling stability (Figure 8d) and rate performance (Figure 8f) of composite S/m-HCNF may be referred to as the superior electrochemical reaction reversibility of elemental sulfur therein.



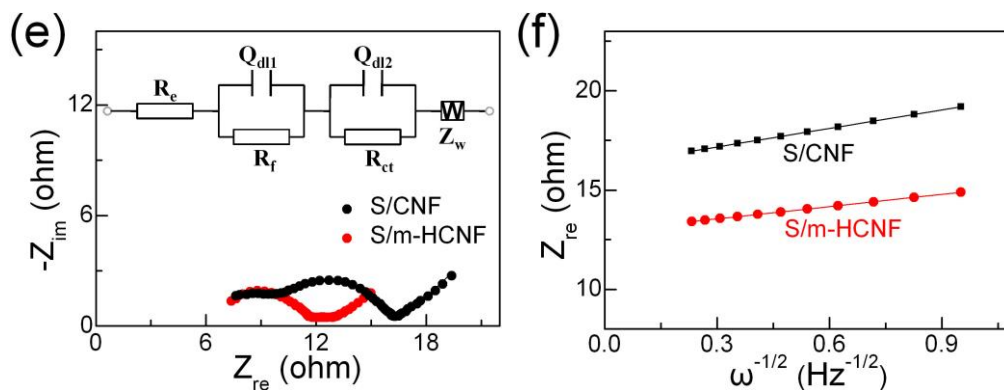


Figure 9. (left) Nyquist plots and (right) the corresponding low-frequency relationships of Z_{re} against $\omega^{-0.5}$ for the comparative S/CNF and S/m-HCNF cathodes: (a, b), at open-circuit voltage; (c, d), after the 10th cycle at 0.5 C; (e, f), after the 100th cycle at 0.5 C. In panel (a), (c) or (e), the fitting results and an equivalent circuit were also inserted.

Insofar as a carbon-doped cathode of Li-S battery is concerned, its carbon-modified electron conductivity (or the internal resistances) and its electrochemical activity (or the inner Li^+ -ion diffusion) may be generally the rate-determining factors. At different electrochemical states, Nyquist plots and the corresponding equivalent circuits and data analyses of composites S/CNF and S/m-HCNF are comparatively revealed in Figure 9, and the relative parameters of electrolyte-solution resistance (R_e), charge-transfer resistance (R_{ct}), surface-film resistance (R_f) are listed in Table 1. The sum of R_{ct} and R_f values can adequately reflect the difficulty of the electrochemical reaction between elemental sulfur and metallic lithium, the value of R_e is proportional to the concentration of Li_2S_n ($4 \leq n \leq 8$) intermediates in electrolyte solution and the Warburg impedance (Z_w) is related to Li^+ -ion diffusion into the bulk of the composite cathode [35, 48, 49].

There is no surface-film boundary formed prior to the electrode reaction between elemental sulfur and metallic lithium, and thus the higher R_{ct} value of S/CNF (77.66 Ω) than that of S/m-HCNF (60.55 Ω) further confirms the superior lithiation-delithiation reversibility of the latter at open-circuit voltage (Figure 9a). Based on the analysis of EIS results, Li^+ -ion diffusion coefficient (D_{Li}) within a lithium-intercalated electrode can be normally estimated according to the following equations[37, 50]:

$$D_{\text{Li}} = 0.5 \left(RT / An^2 F^2 \sigma C \right)^2 \quad (1)$$

$$Z_{re} = R_e + R_{ct} + \sigma \omega^{-0.5} \quad (2)$$

Where, R is the gas constant (8.314 J mol⁻¹ K⁻¹); T is the Kelvin temperature (298.2 K); A is the area of the cathode/electrolyte interface; n is electron number for each molecule during Li^+ -ion insertion; F is the Faraday's constant (96500 C mol⁻¹); C is the molar concentration of lithium ions for the solid-state electrode; σ is the Warburg impedance coefficient which has the relationship with Z_{re} ; and ω is the angular frequency in the low frequency range.

As for a carbonaceous composite cathode (i.e., a non-lithium-intercalated electrode) of Li-S battery, Li^+ -ion concentration in the electrolyte has been used to calculate Li^+ -ion diffusion coefficient D_{Li} within the bulk electrode at open-circuit voltage [7, 22, 35, 36]. Especially, therein these values of D_{Li} , estimated according to equation (1), are at the 10^{-8} - 10^{-10} order of magnitude, which are too big to

reflect the real electrochemical activity of elemental sulfur. If the concentration of molecular S_8 in the membrane-like electrode determines its reaction rate with metallic lithium, S_8 concentration might be able to substitute for the effective activity of Li^+ -ion within the solid-state cathode of composite S/CNF or S/m-HCNF. That is, based on the density (ρ) of carbon-sulfur composite S/CNF (or S/m-HCNF) and the molecular weight of S_8 (M), in equation (1) the value of parameter C could be “precisely” calculated as $3.58 \times 10^{-4} \text{ mol cm}^{-3}$ (or $1.60 \times 10^{-3} \text{ mol cm}^{-3}$).

When Li^+ -ion diffusion within a lithium-intercalated electrode is rate-determining, the relationship between Z_{re} and the root square angular frequency $\omega^{-0.5}$ is linear in a low frequency region. As shown in Figure 9b, at open-circuit voltage the slope of each fitting line (i.e., parameter σ) is 30.7122 or 6.2603 $\Omega \text{ cm}^2 \text{ s}^{-0.5}$, correspondingly giving the D_{Li} value of 3.51×10^{-15} or $4.21 \times 10^{-15} \text{ cm}^2 \text{ s}^{-1}$ for S/CNF or S/m-HCNF composite. By comparison, the D_{Li} in S/m-HCNF electrode is ~ 1.2 times as big as that in bulk S/CNF, which can be reasonably attributed to the shorter Li^+ -ion diffusion path for mesoporous structure of S/m-HCNF.

After 10 or 100 charge-discharge cycles at 0.5 C, the gradual increase of R_e value and the emerging of high-frequency R_f semi-circle could be detected by Nyquist plot (Figure 9c or 9e). By comparison with the situation at open-circuit voltage, the increase of R_e value can be attributed to the gradual formation of electrolyte-soluble Li_2S_n ($4 \leq n \leq 8$), while the sharp decrease of $R_{ct} + R_f$ value may be assigned to the penetration of electrolyte solution into the bulk electrode (Table 1). As shown in Table 1, the $R_{ct} + R_f$ value of S/CNF electrode is always bigger than that of S/m-HCNF cathode under each electrochemical state, and these are consistent with the comparative cycling- and rate-performance results shown in Figure 8c-f.

Table 1. A summary of electrochemical parameters (i.e., R_e , R_f , R_{ct} and $R_f + R_{ct}$) and corresponding chi-square test coefficient (i.e., χ^2) obtained according to EIS results and the applied equivalent circuit presented in Figure 9a, 9c and 9e.

Electrodes (Electrochemical state)	R_e / Ω	R_f / Ω	R_{ct} / Ω	$(R_f + R_{ct}) / \Omega$	χ^2
S/CNF (fresh)	2.63	-	77.66	80.29	5.34×10^{-4}
S/m-HCNF (fresh)	2.94	-	60.55	63.49	4.05×10^{-4}
S/CNF (10th)	3.78	3.81	9.19	13.00	2.66×10^{-5}
S/m-HCNF (10th)	3.39	3.02	3.76	6.78	6.34×10^{-5}
S/CNF (100th)	6.61	2.61	7.03	9.64	5.93×10^{-5}
S/m-HCNF (100th)	6.43	3.96	3.07	7.03	3.35×10^{-5}

As revealed in Figure 9d or 9f, after the 10th or 100th cycle at 0.5 C, the fitted σ values are 1.8667 (or 3.1236) and 1.9205 (or 2.0559) $\Omega \text{ cm}^2 \text{ s}^{-0.5}$, which corresponds to the D_{Li} values of 9.51×10^{-13} (or 3.40×10^{-13}) and 4.47×10^{-14} (or 3.90×10^{-14}) $\text{cm}^2 \text{ s}^{-1}$ for S/CNF and S/m-HCNF, respectively. Within each solid-state electrode, the sharp decrease of D_{Li} value from the open-circuit voltage to the state after 10th cycle could be simply explained by the penetration of electrolyte solution, whereas the slight decrease of D_{Li} value from the state after the 10th cycle to the state after

the 100th cycle could be interpreted using the shuttling effect of the electrolyte-soluble Li_2S_n ($4 \leq n \leq 8$) intermediates. Comparing the D_{Li} values obtained from Figure 9d with those calculated from Figure 9f shows that the D_{Li} values of S/m-HCNF and S/CNF composite electrodes decrease by 12.8% and 64.3% in sequence. These further indicate a superior lithiation-delithiation reversibility of elemental sulfur in composite S/m-HCNF.

4. CONCLUSIONS

In summary, cross-linked nanofiber webs of PPy-NF were used as precursors to prepare cross-linked carbon nanofiber (CNF, BET area $\sim 192.5 \text{ m}^2 \text{ g}^{-1}$) and mesoporous hydroxylated carbon nanofiber (m-HCNF, BET area $\sim 1808.9 \text{ m}^2 \text{ g}^{-1}$) via a simple carbonization and a combined carbonization/activation method, respectively. When serving as a conductive matrix to impregnate molecular S_8 , the mesoporous structure of m-HCNF (pore volume $\sim 1.77 \text{ cm}^3 \text{ g}^{-1}$; pore diameter $\sim 3.3 \text{ nm}$) could load a 62.0% weight percentage of elemental sulfur, higher than that of non-porous CNF (sulfur loading 47%, pore volume $\sim 0.42 \text{ cm}^3 \text{ g}^{-1}$). Especially, S_8 crystallites localize at the surface of CNF cross-linked nanofiber scaffolds, whereas amorphous sulfur was mostly and uniformly distributed within the m-HCNF mesoporous frameworks.

When applied as a Li-S battery cathode, S/m-HCNF composite electrode shows a reversible capacity of 884.1 mAh g^{-1} after 150 cycles at 0.5 C, which is superior to that of S/CNF cathode (599.3 mAh g^{-1} , 150th, 0.5C). Even at a constant dosage of electrolyte (30 mL) per gram of sulfur, the R_e value of S/m-HCNF is smaller than that of S/CNF under each electrochemical state (e.g., after the 100th cycle at 0.5 C, the latter $\sim 6.61 \text{ } \Omega >$ the former $\sim 6.43 \text{ } \Omega$), and so does the sum of $R_{\text{ct}} + R_{\text{f}}$ value (e.g., after the 100th cycle at 0.5 C, the latter $\sim 9.65 \text{ } \Omega >$ the former $\sim 7.03 \text{ } \Omega$). The enhanced reaction reversibility of S_8 in composite S/m-HCNF with metallic lithium could relate both to the mesoporous structure of the carbonaceous scaffold (i.e., the short Li^+ -ion diffusion pathway) and to the low concentration of electrolyte-soluble Li_2S_n ($4 \leq n \leq 8$) intermediates (i.e., the slight shuttling effect or the low R_e value). Importantly, these coincide well with the comparative values of Li^+ -ion diffusion coefficient D_{Li} estimated according to the concentration of molecular S_8 , and as an example, at open-circuit voltage the D_{Li} value of cathode S/m-HCNF ($4.21 \times 10^{-15} \text{ cm}^2 \text{ s}^{-1}$) is bigger than that of solid-state S/CNF ($3.51 \times 10^{-15} \text{ cm}^2 \text{ s}^{-1}$).

ACKNOWLEDGEMENTS

Authors thank the financial supports from the National Natural Science Foundation of China (21673131), from the Taishan Scholar Project of Shandong Province (ts201511004), from the Natural Science Foundation of Shandong Province (ZR2016BM03).

References

1. Y. Yang, G. Zheng, Y. Cui, *Chem. Soc. Rev.*, 42 (2013) 3018-3032.
2. X. Liang, C. Hart, Q. Pang, A. Garsuch, T. Weiss, L.F. Nazar, *Nat. Commun.*, 6 (2015) 5682.
3. S. Evers, L.F. Nazar, *Acc. Chem. Res.*, 46 (2013) 1135-1143.

4. A. Manthiram, S.-H. Chung, C. Zu, *Adv. Mater.*, 27 (2015) 1980-2006.
5. L. Qie, C. Zu, A. Manthiram, *Adv. Energy Mater.*, 6 (2016) 1502459.
6. Q. Pang, L.F. Nazar, *ACS Nano*, 10 (2016) 4111-4118.
7. H. Wu, L. Xia, J. Ren, Q. Zheng, C. Xu, D. Lin, *J. Mater. Chem. A*, 5 (2017) 20458-20472.
8. Y. Chen, X. Li, K.-S. Park, J. Hong, J. Song, L. Zhou, Y.-W. Mai, H. Huang, J.B. Goodenough, *J. Mater. Chem. A*, 2 (2014) 10126-10130.
9. W. Zhou, Y. Yu, H. Chen, F.J. DiSalvo, H.D. Abruña, *J. Am. Chem. Soc.*, 135 (2013) 16736-16743.
10. Y. Mi, W. Liu, K.R. Yang, J. Jiang, Q. Fan, Z. Weng, Y. Zhong, Z. Wu, G.W. Brudvig, V.S. Batista, H. Zhou, H. Wang, *Angew. Chem. Int. Ed.*, 55 (2016) 14818-14822.
11. F. Chen, J. Yang, T. Bai, B. Long, X. Zhou, *Electrochim. Acta*, 192 (2016) 99-109.
12. R. Fang, S. Zhao, S. Pei, X. Qian, P.-X. Hou, H.-M. Cheng, C. Liu, F. Li, *ACS Nano*, 10 (2016) 8676-8682.
13. B. Zhang, M. Xiao, S. Wang, D. Han, S. Song, G. Chen, Y. Meng, *ACS Appl. Mater. Interfaces*, 6 (2014) 13174-13182.
14. Z. Li, Y. Jiang, L. Yuan, Z. Yi, C. Wu, Y. Liu, P. Strasser, Y. Huang, *ACS Nano*, 8 (2014) 9295-9303.
15. J. Jia, K. Wang, X. Zhang, X. Sun, H. Zhao, Y. Ma, *Chem. Mater.*, 28 (2016) 7864-7871.
16. Q. Fan, W. Liu, Z. Weng, Y. Sun, H. Wang, *J. Am. Chem. Soc.*, 137 (2015) 12946-12953.
17. T. Chen, B. Cheng, G. Zhu, R. Chen, Y. Hu, L. Ma, H. Lv, Y. Wang, J. Liang, Z. Tie, Z. Jin, J. Liu, *Nano Lett.*, 17 (2017) 437-444.
18. Q. Pang, J. Tang, H. Huang, X. Liang, C. Hart, K.C. Tam, L.F. Nazar, *Adv. Mater.*, 27 (2015) 6021-6028.
19. X.-X. Peng, Y.-Q. Lu, L.-L. Zhou, T. Sheng, S.-Y. Shen, H.-G. Liao, L. Huang, J.-T. Li, S.-G. Sun, *Nano Energy*, 32 (2017) 503-510.
20. Z. Li, C. Li, X. Ge, J. Ma, Z. Zhang, Q. Li, C. Wang, L. Yin, *Nano Energy*, 23 (2016) 15-26.
21. D. Guo, X.a. Chen, H. Wei, M. Liu, F. Ding, Z. Yang, K. Yang, S. Wang, X. Xu, S. Huang, *J. Mater. Chem. A*, 5 (2017) 6245-6256.
22. M. Chen, S. Jiang, C. Huang, X. Wang, S. Cai, K. Xiang, Y. Zhang, J. Xue, *ChemSusChem*, 10 (2017) 1803-1812.
23. Y. Tan, Z. Zheng, S. Huang, Y. Wang, Z. Cui, J. Liu, X. Guo, *J. Mater. Chem. A*, 5 (2017) 8360-8366.
24. J. Zhang, C.-P. Yang, Y.-X. Yin, L.-J. Wan, Y.-G. Guo, *Adv. Mater.*, 28 (2016) 9539-9544.
25. Y.-J. Li, J.-M. Fan, M.-S. Zheng, Q.-F. Dong, *Energy Environ. Sci.*, 9 (2016) 1998-2004.
26. J. He, L. Luo, Y. Chen, A. Manthiram, *Adv. Mater.*, 29 (2017) 1702707.
27. X. Yang, N. Yan, W. Zhou, H. Zhang, X. Li, H. Zhang, *J. Mater. Chem. A*, 3 (2015) 15314-15323.
28. Z. Wang, L. Qie, L. Yuan, W. Zhang, X. Hu, Y. Huang, *Carbon*, 55 (2013) 328-334.
29. X. Yang, W. Zou, Y. Su, Y. Zhu, H. Jiang, J. Shen, C. Li, *J. Power Sources*, 266 (2014) 36-42.
30. J. Yang, J. Xie, X. Zhou, Y. Zou, J. Tang, S. Wang, F. Chen, L. Wang, *J. Phys. Chem. C*, 118 (2014) 1800-1807.
31. J. Zhang, Z. Zhang, Q. Li, Y. Qu, S. Jiang, *J. Electrochem. Soc.*, 161 (2014) A2093-A2098.
32. J.S. Lee, A. Manthiram, *J. Power Sources*, 343 (2017) 54-59.
33. J.S. Lee, W. Kim, J. Jang, A. Manthiram, *Adv. Energy Mater.*, 7 (2017) 1601943.
34. J.S. Lee, J. Jun, J. Jang, A. Manthiram, *Small*, 13 (2017) 1602984.
35. X. Yang, Y. Yu, N. Yan, H. Zhang, X. Li, H. Zhang, *J. Mater. Chem. A*, 4 (2016) 5965-5972.
36. G. Zhou, H. Tian, Y. Jin, X. Tao, B. Liu, R. Zhang, Z.W. Seh, D. Zhuo, Y. Liu, J. Sun, J. Zhao, C. Zu, D.S. Wu, Q. Zhang, Y. Cui, *P. Natl. Acad. Sci.*, 114 (2017) 840-845.
37. M. Zhang, R. Liu, F. Feng, S. Liu, Q. Shen, *J. Phys. Chem. C*, 119 (2015) 12149-12156.
38. Y. Li, B. Zou, C. Hu, M. Cao, *Carbon*, 99 (2016) 79-89.
39. F. Yu, Y. Li, M. Jia, T. Nan, H. Zhang, S. Zhao, Q. Shen, *J. Alloys Compd.*, 709 (2017) 677-685.

40. K. Yang, Q. Gao, Y. Tan, W. Tian, W. Qian, L. Zhu, C. Yang, *Chem. Eur. J.*, 22 (2016) 3239-3244.
41. R. Chen, T. Zhao, J. Lu, F. Wu, L. Li, J. Chen, G. Tan, Y. Ye, K. Amine, *Nano Lett.*, 13 (2013) 4642-4649.
42. X. Yuan, L. Wu, X. He, K. Zeinu, L. Huang, X. Zhu, H. Hou, B. Liu, J. Hu, J. Yang, *Chem. Eng. J.*, 320 (2017) 178-188.
43. C. Wang, X. Wang, Y. Wang, J. Chen, H. Zhou, Y. Huang, *Nano Energy*, 11 (2015) 678-686.
44. L. Zhang, L. Ji, P.-A. Glans, Y. Zhang, J. Zhu, J. Guo, *Phys. Chem. Chem. Phys.*, 14 (2012) 13670-13675.
45. Z. Li, L. Yin, *ACS Appl. Mater. Interfaces*, 7 (2015) 4029-4038.
46. D. Aurbach, E. Pollak, R. Elazari, G. Salitra, C.S. Kelley, J. Affinito, *J. Electrochem. Soc.*, 156 (2009) A694-A702.
47. J. Schuster, G. He, B. Mandlmeier, T. Yim, K.T. Lee, T. Bein, L.F. Nazar, *Angew. Chem. Int. Ed.*, 51 (2012) 3591-3595.
48. H. Zhang, D. Jia, Z. Yang, F. Yu, Y. Su, D. Wang, Q. Shen, *Carbon*, 122 (2017) 547-555.
49. R. Liu, S. Zhao, M. Zhang, F. Feng, Q. Shen, *Chem. Commun.*, 51 (2015) 5728-5731.
50. Y. Yang, W. Xu, R. Guo, L. Liu, S. Wang, D. Xie, Y. Wan, *J. Power Sources*, 269 (2014) 15-23

© 2018 The Authors. Published by ESG (www.electrochemsci.org). This article is an open access article distributed under the terms and conditions of the Creative Commons Attribution license (<http://creativecommons.org/licenses/by/4.0/>).